Two-Dimensional Layered Structures of Group-V Elements as Transparent Conductors: Insight from a First-Principles Study

Gurudayal Behera,[1] Jiban Kangsabanik,[2,3] Brahmananda Chakraborty,[4,5] K.R. Balasubramaniam,[1,*] and Aftab Alam[3,†]

[1] *Department of Energy Science and Engineering, IIT Bombay, Powai, Mumbai, 400076, India*
[2] *Department of Physics, Technical University of Denmark, 2800 Kongens Lyngby, Denmark*
[3] *Department of Physics, Indian Institute of Technology, Bombay, Powai, Mumbai, 400076, India*
[4] *Homi Bhabha National Institute, Trombay, Mumbai, 400085, India*
[5] *High Pressure & Synchrotron Radiation Physics Division, Bhabha Atomic Research Centre, Trombay, Mumbai, 400085, India*

(Received 9 May 2022; revised 14 April 2023; accepted 21 April 2023; published 22 May 2023)

Exotic optoelectronic and transport properties of two-dimensional (2D) materials have made them the focus of several application-oriented studies. This work is a feasibility study of such 2D structures based on group-V elements as passivating/transparent conducting interlayers in photovoltaic applications. We present a detailed first-principles study of the optoelectronic and carrier-transport properties of the two most stable and experimentally synthesized allotropes (α and β) of As, Sb, and Bi. Monolayers of both allotropes exhibit a band gap for all three elements, which decreases and eventually disappears beyond a critical number of layers (thickness). Interestingly, this transition from semiconducting to metallic behavior is found to be very different for As as compared with Sb and Bi. α-Arsenene remains semiconducting until the pentalayered structure, while β-arsenene becomes metallic beyond the bilayered structure. All other allotropes of Sb and Bi are semiconducting only for a monolayer. The in-plane conductivity of the monolayered structures lies in the range from 10^4 to 10^5 S m^{-1}, and increases with increasing layer thickness. On the other hand, the monolayers exhibit the lowest reflectivity (5% or less), which increases to more than 25%, 50%, and 40% in the visible region for pentalayers of α- and β-arsenene, antimonene, and bismuthene, respectively. Trilayered α-arsenene, with a figure of merit (T^{10}/R_{sh}) of approximately 0.15 mS, is a promising candidate as a transparent conducting layer in solar-cell applications. Such combined evaluation of 2D materials based on their optoelectronic and transport properties is quite useful for future experimental investigations.

DOI: 10.1103/PhysRevApplied.19.054068

I. INTRODUCTION

In recent years, two-dimensional (2D) quantum materials have been studied extensively due to their suitability in various electronic and optoelectronic devices. To name a few, graphene, single-layered or few-layered transition-metal dichalcogenides, black phosphorus, oxides, and mixed carbides have attracted a great deal of attention due to their potential use in electronic devices, composites, energy storage, and sensing [1–11]. Since the discovery of graphene [4,12,13], much attention has been devoted to exploring 2D single-layered monoelemental materials of this class. This is because of their attractive physical and chemical properties, including band-gap tunability, high electrical conductivity, and high mechanical strength. In the past few years, 2D crystals derived from a family of group-V elements, e.g., P, As, Sb, and Bi, have attracted increasing research interest [2,5,14–19]. Among the various group-V 2D monolayers, the first and most explored is phosphorene. Its band gap ranges from 0.3 eV (in bulk) to 2 eV (in monolayers), and coupled with high hole mobility (more than 10^4 cm^2 V^{-1} s^{-1}), it is an interesting material for electronic device applications [20–23]. Other group-V elements based on 2D materials such as arsenene, antimonene, and bismuthene have also been reported to show some intriguing electrical and optoelectronic properties [5,14,15,24].

Recent phonon-dispersion studies have shown that allotropes of group-V 2D structures are dynamically stable with band gaps ranging from 1 to 2.5 eV [14–16,24]. Additionally, Zhang *et al.* [15,24] found that these allotropes of group-V 2D structures exhibit high carrier mobilities (more than 10^3 cm^2 V^{-1} s^{-1}), which render them potential

*bala.ramanathan@iitb.ac.in
†aftab@iitb.ac.in

candidates for different applications, e.g., as a photocathode in photocatalytic water splitting [14,15], topological insulators [2,25], and thermoelectric technologies [26,27]. Also, optical studies [28,29] have revealed that the reflectivity of these 2D structures is low and absorption is almost negligible in the visible region. This combination of the optical and electrical characteristics of these materials makes them potential candidates for passivating and transparent conducting layers for photovoltaic (PV) applications. In this regard also, there are some suggestions in the literature [28–31], albeit the implementation of a specific material as an interlayer in a PV cell and its exact functionality in the device is still nebulous, i.e., whether it can be an appropriate candidate as a transparent conducting layer, a passivating layer, a carrier-transport layer, or a combination of both providing passivation and carrier transport layer to solar photovoltaic devices.

Such monolayers and multilayers must be transparent in the visible region of the solar spectrum and have high electrical conductivity to be used in PV cells. However, these characteristics are highly dependent on their thickness. Also, it is experimentally difficult to maintain the uniformity of such thin layered structures, and only a few sophisticated techniques, such as molecular-beam epitaxy [32,33], mechanical exfoliation [22,34], and plasma-assisted processes [17,35], have been demonstrated in the literature. Therefore, an optimum thickness of the layered structure needs to be determined for its practical use as a transparent conducting layer in a PV cell.

In this article, we report the detailed electronic structure and optical properties of these 2D materials using first-principles density-functional-theory (DFT) calculations. This allows an estimation of the feasibility of monolayers and multilayers of the group-V-element α and β allotropes as passivating/transparent conducting interlayers in solar cells. Among multilayers, we simulate up to a pentalayer of the α and β allotropes of arsenene, antimonene, and bismuthene surface slabs. This covers a thickness up to 28.25 Å. The monolayers of all the elements are found to be semiconducting, the band gap decreases as the layer thickness increases, and after a certain thickness, the material becomes metallic. The optical simulation reveals an extremely low absorption coefficient and extremely low reflectivity for the monolayers, which increases gradually with increasing layer thickness. We further calculate the in-plane conductivity of all the group-V 2D materials using the semiclassical Boltzmann transport equation. Both optical transparency (in the visible region) and electrical conductivity depend on the layer thickness of these 2D materials.

II. COMPUTATIONAL DETAILS

First-principles calculations are performed using DFT [36] as implemented within the Vienna Ab initio Simulation Package [37–39] with a projector-augmented-wave basis [40]. The generalized-gradient-approximation [41] functional as parameterized by the Perdew-Burke-Ernzerhof exchange-correlation potential [42] is used. For a more-accurate calculation of the electronic structure (band gap), the HSE06-screened-hybrid-functional method [43,44] is used. The van der Waals interactions are incorporated in all the calculations with use of the DFT-D2 method of Grimme [45]. The kinetic energy cutoff for the plane-wave basis set is set to 550 eV. The Brillouin-zone integration is done with a Γ-centered scheme with $16 \times 16 \times 1$ **k**-point mesh sampling. The density of states (DOS) is calculated by the tetrahedron method with Blöch corrections [46]. For the HSE06 method, the electronic band structure within is simulated with use of a $6 \times 6 \times 1$ **k**-point mesh for energy convergence. All the atoms in the unit cell are fully relaxed by means of the conjugate-gradient method until the force (energy) converges below 0.001 eV/Å (10^{-6} eV). The constructed supercell slabs are periodic in the x-y plane and are separated by a vacuum of 15 Å in the z direction (perpendicular to the plane) to avoid interaction between the repeated surface-slab geometry.

To calculate the optical properties, the frequency-dependent dielectric constants are calculated by DFT with the random-phase approximation [47–49], as implemented in the Vienna Ab initio Simulation Package. The thickness-dependent exciton binding energies are calculated with the Bethe-Salpeter equation (BSE) [50,51]. All the *GW* and BSE calculations are done with the Tamm-Dancoff approximation method [52,53]. **k**-point-mesh convergence is carefully checked for all the calculations, and finally a Γ-centered $12 \times 12 \times 1$ **k**-point mesh with plane-energy cutoff of 550 eV is used. For *GW* calculations, 36 unoccupied bands are taken into account, while for BSE calculations, 40 bands are considered. Electrical conductivity (σ) and the carrier relaxation time (τ) are calculated with AMSET [54]. Two different scattering mechanisms are considered to calculate the relaxation time: acoustic-deformation-potential scattering (ADP) and ionized-impurity scattering. The effect of optical phonon scattering is not considered in the present case. Further theoretical descriptions of optical and transport properties are given in Sec. 1 in Supplemental Material [55]; also see Refs. [56–61].

III. RESULTS and DISCUSSION

A. Electronic structure of group-V 2D monolayers

The α and β allotropes of arsenene, antimonene, and bismuthene can be constructed by cleaving the surface slabs along the (110) and (111) planes of the rhombohedral bulk As, Sb, and Bi crystals. Figure 1 shows the prototype crystal structures of the α and β allotropes of the group-V 2D monolayer. The α allotropes are arranged in a 2D rectangular lattice with a puckered surface with space group *Pmna* and with four atoms per unit cell. Each monolayer

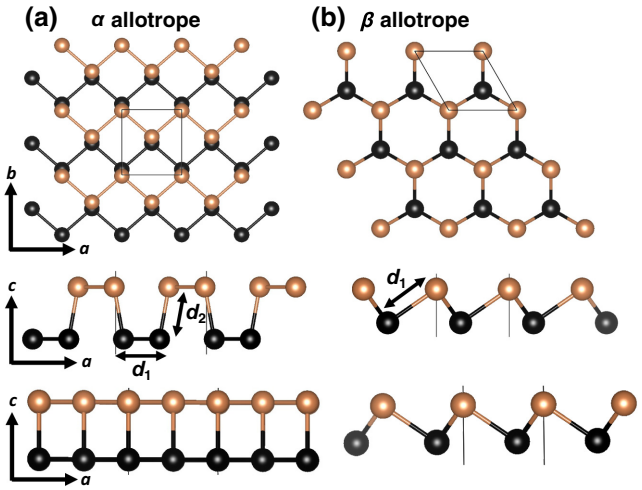

FIG. 1. Prototype 2D crystal structures of (a) α and (b) β allotropes of arsenene, antimonene, and bismuthene along three different projections, i.e., (001), (100), and (010), of the 2D lattice. Atoms at the top and bottom of nonplanar layers are distinguished by different colors. Atoms placed at the bottom of the sublayer are indicated in black, while those at the top are indicated in brown. d_1 and d_2 are the in-plane bond length and the out-of-plane bond length, respectively.

consists of two sublayers, where atoms positioned in the same sublayer are not in the same plane. The two different sublayer atoms are indicated by two different colors in Fig. 1. Similarly, the stable configuration of the β allotrope has a buckled atomic structure with a hexagonal 2D lattice with space group $P\bar{3}m1$ and contains two atoms in each unit cell. Similarly to the α phase, two atomic sublayers exist in the β allotrope. The calculated lattice parameters, bond lengths, and band gaps of monolayered arsenene, antimonene, and bismuthene are given in Table I.

The values of the theoretically optimized lattice parameters of the two allotropes of the three materials match fairly well with experimental values [17,24,62,63] and other theoretically reported values [14,16,28]. The calculated in-plane and out-of-plane bond lengths of α-arsenene, α-antimonene, and α-bismuthene are slightly different from each other. The crystal structures of the α allotropes are anisotropic in the a and b directions, while those of the β allotropes are isotropic, i.e., $a = b$. The layer width (h) of the two sublayers of the α and β allotropes of the three materials is also given in Table I; the values agree reasonably well with previously reported values [14,16,28].

Figure 2 shows the electronic band structures of all the group-V 2D-monolayer allotropes, obtained with use of the HSE06 hybrid functional. The high-symmetry directions of the Brillouin zones for the α and β phases in which the band structures are calculated are shown in Figs. 2(d) and 2(h), respectively. Monolayered α-arsenene and α-antimonene are indirect-band-gap semiconductors, having band gaps of 1.51 and 1.04 eV, respectively. As is evident from Figs. 2(a) and 2(b), the valence-band maximum (VBM) is located in the Γ-X direction, while the conduction-band minimum (CBM) lies at the Γ point. However, α-bismuthene shows a direct band gap of 0.27 eV, where the VBM and the CBM are both located in the Γ-X direction [see Fig. 2(c)]. The β allotropes of arsenene and antimonene also show an indirect band gap, with values of 2.28 and 1.85 eV, respectively, where the CBM is located in the Γ-M direction, while the VBM lies at the Γ point [see Figs. 2(e) and 2(f)]. β-Bismuthene is also a direct-band-gap semiconductor, with a band gap of 0.95 eV [see Fig. 2(g)], where both the VBM and the CBM lie at the Γ point. Our calculated band structures for both allotropes of arsenene, antimonene, and bismuthene match fairly well with those in previous studies [15,16,28].

The in-plane and out-of-plane bond lengths increase on increase of the atomic number. For example, as seen from Table I, the in-plane bond length (d_1) of α-As, α-Sb, and

TABLE I. Calculated lattice parameters, bond lengths, layer width, and band gaps of α and β allotropes of monolayered arsenene, antimonene, and bismuthene. Perdew-Burke-Ernzerhof (PBE).

Allotrope	Lattice parameters (Å)	Bond lengths (Å)	Layer width (h) (Å)	Band gap (eV) PBE method	HSE06 method	Expt.
α-Arsenene	$a = 3.70, b = 4.76$ $a = 3.65, b = 4.74$ (expt. [24])	$d_1 = 2.50, d_2 = 2.48$	2.38	0.79	1.51	1.0 [24]
α-Antimonene	$a = 4.36, b = 4.89$	$d_1 = 2.91, d_2 = 2.83$	2.79	0.32	1.04	0.85 [62]
α-Bismuthene	$a = 4.59, b = 5.01$	$d_1 = 3.08, d_2 = 2.98$	2.95	0.07	0.27	0.15 [63]
β-Arsenene	$a = b = 3.61$ $a = b = 3.60$ (expt. [17])	$d_1 = 2.50$	1.40	1.60	2.28	1.42 [17]
β-Antimonene	$a = b = 4.12$	$d_1 = 2.89$	1.64	1.26	1.85	2 [62]
β-Bismuthene	$a = b = 4.34$ $a = b = 4.47$ (expt. [63])	$d_1 = 3.04$	1.71	0.54	0.95	0.33 [63]

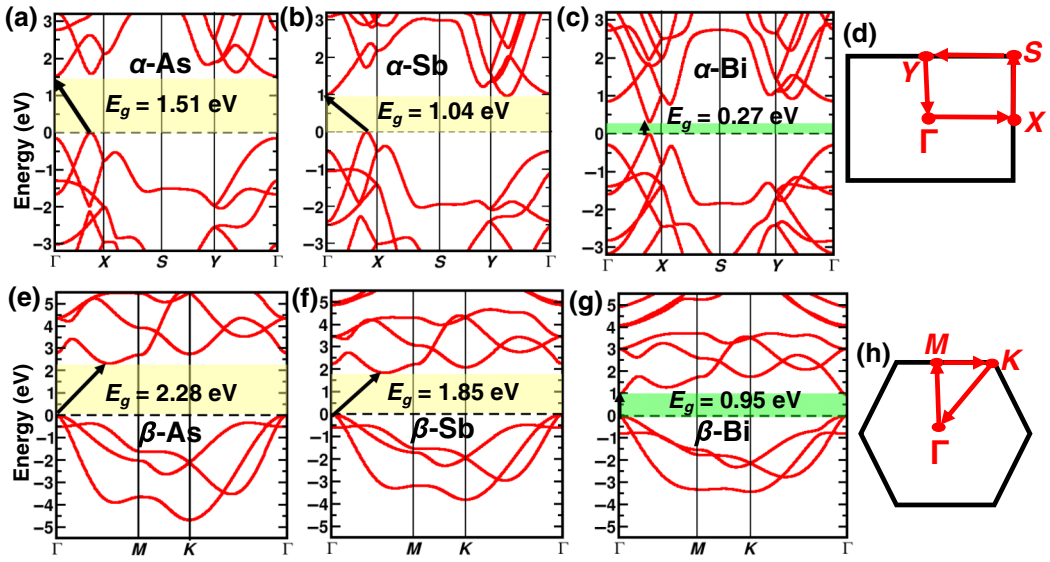

FIG. 2. Electronic band structures of (a) α-arsenene, (b) α-antimonene, (c) α-bismuthene, (e) β-arsenene, (f) β-antimonene, and (g) β-bismuthene, calculated with use of the HSE06 hybrid functional. The band gap (E_g) for each case is indicated in the respective plot. The Fermi level (E_F) is set to 0 eV. (d),(h) Brillouin zones and the high-symmetry directions for the α and β phases.

α-Bi is 2.5, 2.91, and 3.08 Å, respectively. Similarly, for β phases, the bond length increases as we move from As to Bi. This is expected as the atomic size increases from As to Bi. The covalent radii of As, Sb, and Bi are 1.15, 1.45, and 1.6 Å, respectively [64]. The ratio of the bond length and the corresponding sum of covalent radii is 1.09 for As, 1.00 for Sb, and 0.96 for Bi. As we move from As to Bi, this ratio decreases, which indicates an increase in hybridization. This stronger hybridization may result in more dispersive bands as we move from As to Bi, and may contribute to the reduction in the band gap. Also, the band gap of the α allotropes is relatively smaller than that of the β allotropes for all three materials. The out-of-plane bond length (d_2) might play an important role in this phenomenon. In the α allotrope of all three 2D crystals, d_2 is smaller than d_1, implying that the out-of-plane atoms are closer and relatively more strongly interactive than the in-plane atoms. Because of this, the orbital hybridization is relatively stronger in the α structures as compared with the β structures. The orbital hybridization is also explained from the projected density of states plots, as explained later. We also study the effect of spin-orbit coupling (SOC) in all our calculations. It does not result in much change in the band gap and band topology (apart from minor splitting) of arsenene and antimonene. Bi, being a heavy element, shows some changes in the band gap. For instance, the band gap for an α-bismuthene monolayer changes from 0.27 eV without SOC to 0.17 eV with SOC, while that of a β-bismuthene monolayer changes from 0.95 eV without SOC to 0.75 eV with SOC. Once again, apart from minor band splitting, the band topology remains unaltered. The effect of such small changes in the band gap on the optoelectronic properties of the monolayer is checked and found to be insignificant. Beyond a monolayer, bismuthene becomes metallic, and hence there are only minor effects on the band topology. The simulated band gaps for the three monolayers cover a wide range, 0.27–2.28 eV, which can be important for electronic and optoelectronic applications.

B. Electronic structure of multilayered α-arsenene, β-arsenene, α-antimonene, β-antimonene, α-bismuthene, and β-bismuthene

The band-structure calculations show that the monolayers of the three group-V 2D materials are semiconductors and have a thickness ranging between 2 and 3 Å. However, synthesizing such thin monolayers is expensive and sophisticated. The transparency, charge transport, and ease of synthesis are thus highly dependent on the thickness of these layered structures. To find an optimal thickness as a passivating and transparent conducting layer for solar PV devices, we further investigate the layer-thickness dependence of the electronic and optical properties of these 2D structures. We choose bilayered to pentalayered surface slabs with a 15-Å vacuum between the repeated slab geometry for all the surfaces. To grow the multilayered systems, we consider only the *AB* stacking between the layers that exists in the stable configuration as per previous literature [65,66]. In *AB* stacking, the top layer is shifted by one half (α-As) or one third (β-As) of the unit cell in the *a* direction of the 2D surfaces. The prototype pentalayer *AB*-stacking relaxed structures of the α and β allotropes are shown in Figs. 3(a) and 3(e). The thickness-dependent electronic band structures showing only VBM and CBM

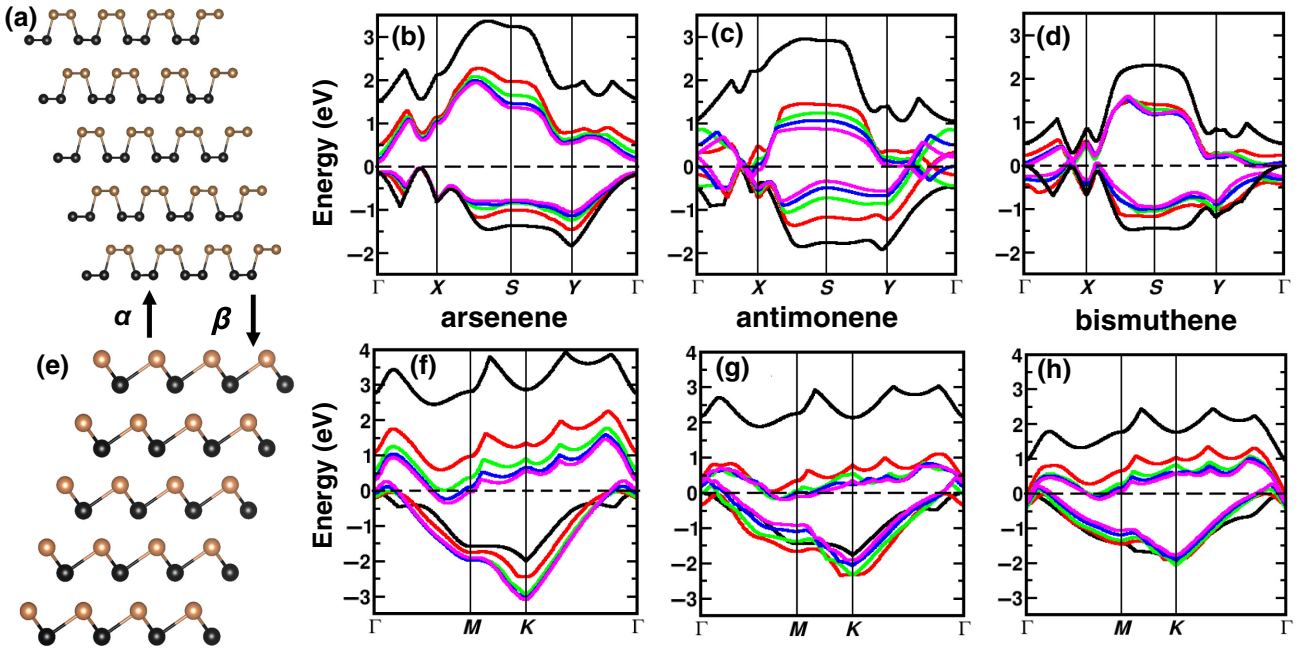

FIG. 3. Model crystal structures of pentalayered (a) α and (e) β allotropes of arsenene, antimonene, and bismuthene. Thickness-dependent band structures showing only conduction-band minima and valence-band maxima for a monolayer (black), bilayer (red), trilayer (green), tetralayer (blue), and pentalayer (magenta) of (b)–(d) α allotropes and (f)–(h) β allotropes. The Fermi level (E_F) is set to 0 eV.

for different layered α and β allotropes of arsenene, antimonene, and bismuthene are shown in Fig. 3. The whole band structures of all the group-V α and β allotropes are provided in Figs. S2.1 and S2.2 in Supplemental Material [55]. The in-plane and out-of-plane bond distances between the atoms for different allotropes with different layer thicknesses (monolayer to pentalayer) are given in Table II. These bond lengths are calculated by our taking an average of the respective bond lengths between different consecutive layers for a given multilayered system. On increase of the layer thickness, the in-plane bond length for all the 2D layers remains the same as for the monolayer throughout the multilayer. In contrast, the out-of-plane bond length in the case of all the α allotropes increases on increase of the layer thickness, which plays a major role in the change in orbital hybridization and hence the electronic, optical, and transport properties.

Table III gives the band gaps and layer widths of the different multilayered group-V 2D surface slabs. Evidently, the band gap decreases with increasing number of layers, eventually becoming metallic after a certain thickness. For α-arsenene, the band gap decreases from 1.51 to 0.05 eV as the layer thickness is increased from a monolayer to a pentalayer. Similarly to monolayered α-arsenene, multilayered α-arsenene has an indirect band gap, where the CBM is located at the Γ point, while the VBM lies at a point in the Γ-X high-symmetry direction [see Fig. 3(b)]. In the case of β-arsenene, the monolayered

TABLE II. Average in-plane (d_1) and out-of-plane (d_2) bond lengths (in Å) of various layered structures of α and β allotropes of arsenene, antimonene, and bismuthene.

Allotrope	Monolayer	Bilayer	Trilayer	Tetralayer	Pentalayer
α-Arsenene	$d_1 = 2.50$	$d_1 = 2.50$	$d_1 = 2.50$	$d_1 = 2.50$	$d_1 = 2.50$
	$d_2 = 2.48$	$d_2 = 2.49$	$d_2 = 2.49$	$d_2 = 2.51$	$d_2 = 2.52$
α-Antimonene	$d_1 = 2.91$	$d_1 = 2.91$	$d_1 = 2.91$	$d_1 = 2.91$	$d_1 = 2.91$
	$d_2 = 2.83$	$d_2 = 2.89$	$d_2 = 2.91$	$d_2 = 2.93$	$d_2 = 2.84$
α-Bismuthene	$d_1 = 3.08$	$d_1 = 3.08$	$d_1 = 3.08$	$d_1 = 3.08$	$d_1 = 3.08$
	$d_2 = 2.98$	$d_2 = 3.00$	$d_2 = 3.01$	$d_2 = 3.02$	$d_2 = 3.02$
β-Arsenene	$d_1 = 2.50$	$d_1 = 2.50$	$d_1 = 2.50$	$d_1 = 2.50$	$d_1 = 2.50$
β-Antimonene	$d_1 = 2.89$	$d_1 = 2.89$	$d_1 = 2.89$	$d_1 = 2.89$	$d_1 = 2.89$
β-Bismuthene	$d_1 = 3.04$	$d_1 = 3.04$	$d_1 = 3.04$	$d_1 = 3.04$	$d_1 = 3.04$

TABLE III. Layer widths and band gaps (or metallicity) of various layered structures of α and β allotropes of arsenene, antimonene, and bismuthene, calculated with use of the HSE06 hybrid functional.

Allotrope	Monolayer		Bilayer		Trilayer		Tetralayer		Pentalayer	
	Layer width (Å)	Band gap (eV)	Layer width (Å)	Band gap (eV)	Layer width (Å)	Band gap (eV)	Layer width (Å)	Band gap (eV)	Layer width (Å)	Band gap (eV)
α-Arsenene	2.38	1.51	7.91	0.5	13.47	0.24	19.05	0.13	24.54	0.05
α-Antimonene	2.79	1.04	9.01	Metal	15.19	Metal	21.36	Metal	27.50	Metal
α-Bismuthene	2.95	0.27	9.52	Metal	15.87	Metal	21.83	Metal	28.25	Metal
β-Arsenene	1.40	2.28	5.74	0.5	10.04	Metal	14.23	Metal	18.26	Metal
β-Antimonene	1.64	1.85	5.81	Metal	9.23	Metal	13.78	Metal	17.56	Metal
β-Bismuthene	1.71	0.95	6.24	Metal	10.91	Metal	15.20	Metal	19.15	Metal

and bilayered structures show semiconducting behavior, with indirect band gaps of 2.28 and 0.5 eV, respectively [see Fig. 3(f)], and beyond these structures the behavior becomes metallic. In contrast, only the monolayer geometry of α-antimonene, β-antimonene, α-bismuthene, and β-bismuthene shows semiconducting behavior, and all the multilayered surface slabs show metallic character [Figs. 3(c), 3(d), 3(g), and 3(h)]. Although the nature of the band structures remains the same as for the monolayer for these 2D materials, the positions of the VBM and CBM are shifted with increasing layer thickness (see Fig. 3). We speculate that this might be due to the rapid surface reconstructions and the semiconductor-to-metallic transitions of all these materials.

Figure 4 shows the orbital projected DOS for different layered α and β allotropes of arsenene. The orbital projected DOS for different layered antimonene and bismuthene allotropes is shown in Fig. S3 in Supplemental Material [55]. In all cases, the significant contribution near the Fermi level (E_F) (comprising both valence and conduction bands) arises from p orbitals (in particular, p_z orbitals). The electronic state of the s orbital is located deep within the valence band, with a very small contribution near the E_F; d orbitals hardly contribute anything near the E_F, as expected. In other words, these group-V 2D materials acquire a strong sp hybridization. The β phases have higher contributions of s orbitals than do α phases. As a result, the sp hybridization in β structures is more significant than in α structures. This strong sp hybridization induces large band gaps of the β structures. As the layer thickness increases, the contribution of s and d orbitals increases in the deep region of valence and conduction bands. The dominant contribution of p_z orbitals is a common feature of 2D materials such as silicene, germanene, and phosphorene, which involves sp^2-like bonding [14]. With increasing number of layers, the electronic states of p_z orbitals mediate interlayer interaction between adjacent layers, resulting in a band dispersion perpendicular to the plane. Consequently, the multilayered structures have smaller band gaps than the monolayers and eventually become metallic after a certain number of layers. Effects of a similar kind are also observed in other 2D materials, such as phosphorene and monolayered transition-metal dichalcogenides [67–69], where the band gap is inversely proportional to the number of layers.

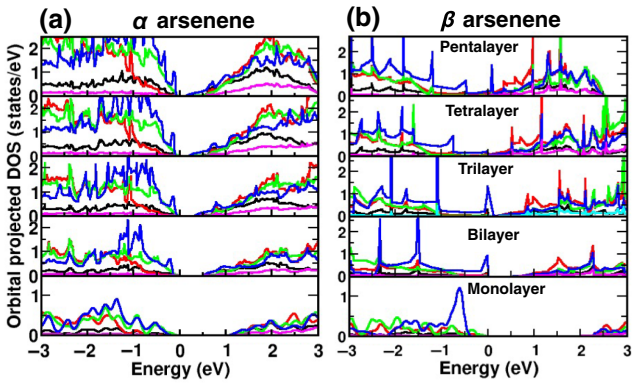

FIG. 4. Orbital projected DOS for a monolayer, bilayer, trilayer, tetralayer, and pentalayer of (a) α-arsenene and (b) β-arsenene. Black, red, green, blue, and magenta lines show the projected DOS for s, p_x, p_y, p_z, and d orbitals, respectively. The Fermi level (E_F) is set to 0 eV.

C. Optical properties of multilayered α-arsenene, β-arsenene, α-antimonene, β-antimonene, α-bismuthene, and β-bismuthene

Here we present the optical properties, i.e., complex dielectric function $\varepsilon(\omega)$, absorption coefficient, and reflectivity, for the multilayered surfaces of three elements calculated with use of the HSE06 functional. The optical properties of all the surface slabs are calculated by our considering incident light with polarization of the electric field in the z direction ($E \parallel z$), i.e., the out-of-plane direction. Figures 5 and 6 show the real [$\varepsilon_1(\omega)$] and imaginary [$\varepsilon_2(\omega)$] parts of the complex dielectric function for α and β allotropes of the three materials with different layer widths. $\varepsilon_1(\omega)$ describes the electronic polarizability of the material, while $\varepsilon_2(\omega)$ is related to the interband transitions

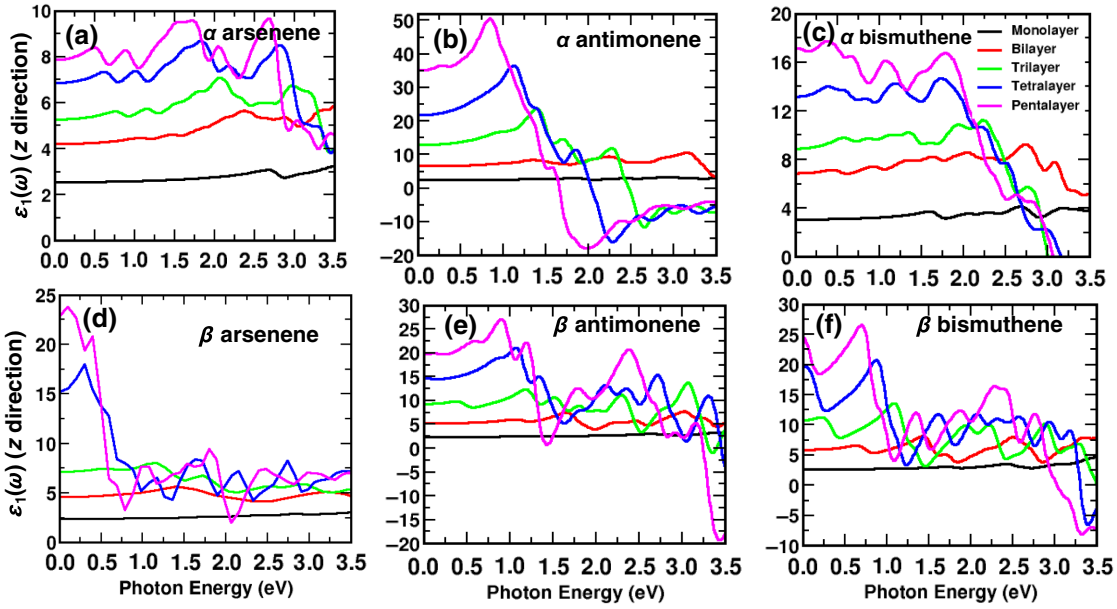

FIG. 5. Real part of the complex dielectric function in the out-of-plane polarization direction ($E \parallel z$) for a monolayer, bilayer, trilayer, tetralayer, and pentalayer of (a)–(c) α and (d)–(f) β allotropes of arsenene, antimonene, and bismuthene, calculated with use of the HSE06 hybrid functional.

due to the absorption of radiation by electrons in occupied valence bands below the Fermi level. The static dielectric constant, i.e., ε_1 at zero photon energy, has finite values for all the 2D layered structures. For example, for monolayered α-arsenene and β-arsenene, ε_1 is 2.54 and 2.42, respectively, as evident from Fig. 5. As the layer width is increased, ε_1 increases (see Fig. 5), suggesting that these materials are highly polarized. The α allotropes have relatively higher polarizability than the β allotropes. The real part of the dielectric function is negative in the energy range between 2.0 and 5.5 eV in the case of α-antimonene and β-antimonene [see Figs. 5(b) and 5(e)]. This indicates the metallic character of the material in this energy range of the electromagnetic spectrum. Similar phenomena are also observed in the case of α-arsenene, β-arsenene, α-bismuthene, and β-bismuthene. The real dielectric constants are negative in the energy range between 5.0 and 9.0 eV for arsenene multilayers and between 3 and 7 eV for bismuthene multilayers.

The imaginary part of the dielectric function $\varepsilon_2(\omega)$, as shown in Fig. 6, for various layered α and β allotropes clearly remains zero in the range of photon energies that is the same as their band gaps. Above this energy range, several peaks are observed in $\varepsilon_2(\omega)$ due to the absorption of incident photons and the interband transition of electrons from the valence band to the conduction band. For monolayers, these peaks are observed in the high-photon-energy range (greater than 3 eV), indicating no absorption of photons in the low-energy range (approximately 0 to 2.5 eV). In other words, most low-energy photons are transmitted due to the small monolayer thickness. All the peaks in $\varepsilon_2(\omega)$ are mainly attributed to the electronic transitions from p states in the valence band to hybridized s or p states in the conduction band (as shown in the orbital projected DOS plot in Fig. 4). With the increase in thickness (number of layers), the peaks are shifted slightly toward the left (lower energy) as compared with the monolayer case. This happens mainly due to the reduction of the band gap with increasing layer thickness. Since the major contribution to $\varepsilon_2(\omega)$ arises from the interband transitions of electrons from the valence band to the conduction band near the Fermi level, and the band gap of the α allotropes follows a trend, i.e., $E_g(\alpha\text{-arsenene}) > E_g(\alpha\text{-antimonene}) > E_g(\alpha\text{-bismuthene})$, so the $\varepsilon_2(\omega)$ curves of α-arsenene are blueshifted as compared with those of α-antimonene and α-bismuthene [see Figs. 6(a)–6(c)]. The observed blueshift in the $\varepsilon_2(\omega)$ curves of β-arsenene as compared with those of β-antimonene and β-bismuthene can be explained in a similar manner [see Figs. 6(d)–6(f)].

The thickness-dependent absorption coefficients of the group-V 2D structures are shown in Fig. 7. A blueshift, as mentioned above, in the $\varepsilon_2(\omega)$ curves is observed in the absorption spectra of α-arsenene (β-arsenene) as compared with those of α-antimonene and α-bismuthene (β-antimonene and β-bismuthene); however, the absorption bandwidth of antimonene and bismuthene is broader than that of arsenene irrespective of their being in the α phase or the β phases. The absorption of both monolayered allotropes is negligible in the visible region, as shown in Fig. 7. On increase of the layer thickness, the absorption coefficient remains negligible in the visible region up to the pentalayered structure in the case of α-arsenene and

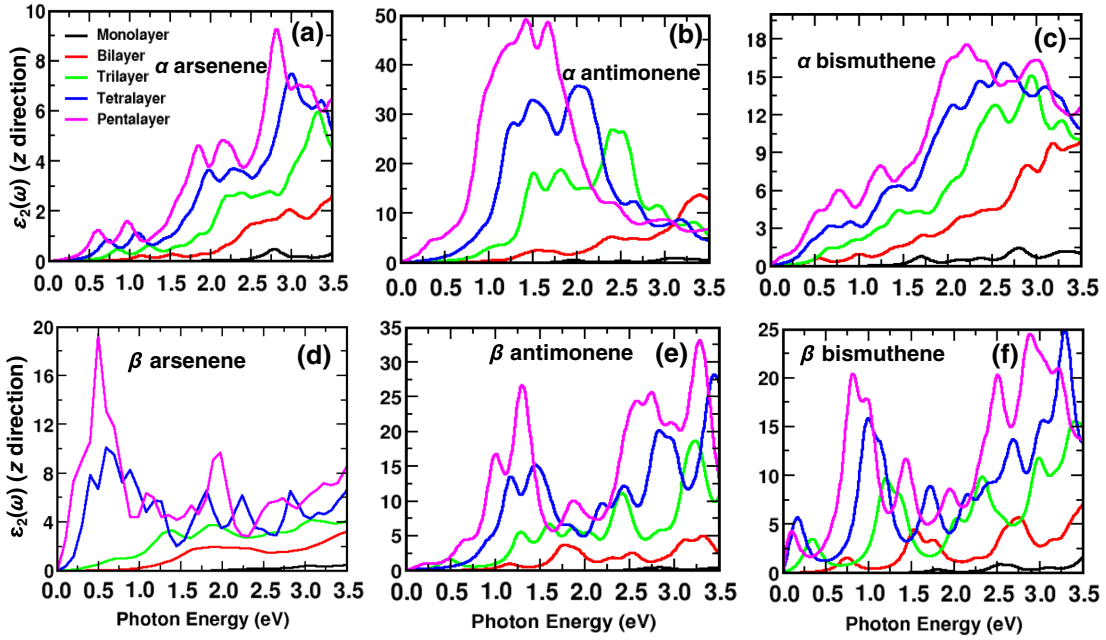

FIG. 6. Imaginary part of the complex dielectric function in the out-of-plane polarization direction ($E \parallel z$) for a monolayer, bilayer, trilayer, tetralayer, and pentalayer of (a)–(c) α and (d)–(f) β allotropes of arsenene, antimonene, and bismuthene, calculated with use of the HSE06 hybrid functional.

α-bismuthene and up to the trilayered structure for α-antimonene. Similarly, the absorption remains negligible for β phases up to the trilayered structure. Above a photon energy of 2 eV, the absorption coefficient increases after the bilayered structure for these group-V 2D structures. Figure 8 depicts the thickness-dependent reflectivity for α

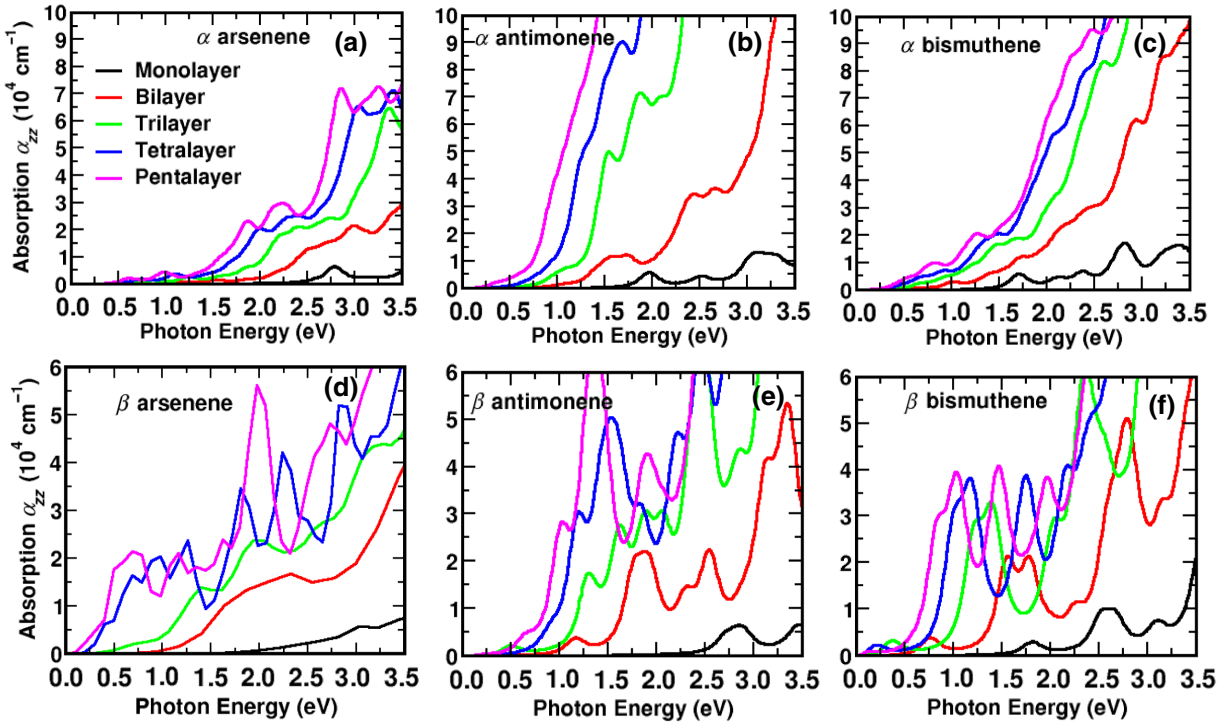

FIG. 7. Absorption coefficient (α) of the out-of-plane polarization for various ilayered structures of (a)–(c) α and (d)–(f) β allotropes of arsenene, antimonene, and bismuthene, calculated with use of the HSE06 hybrid functional.

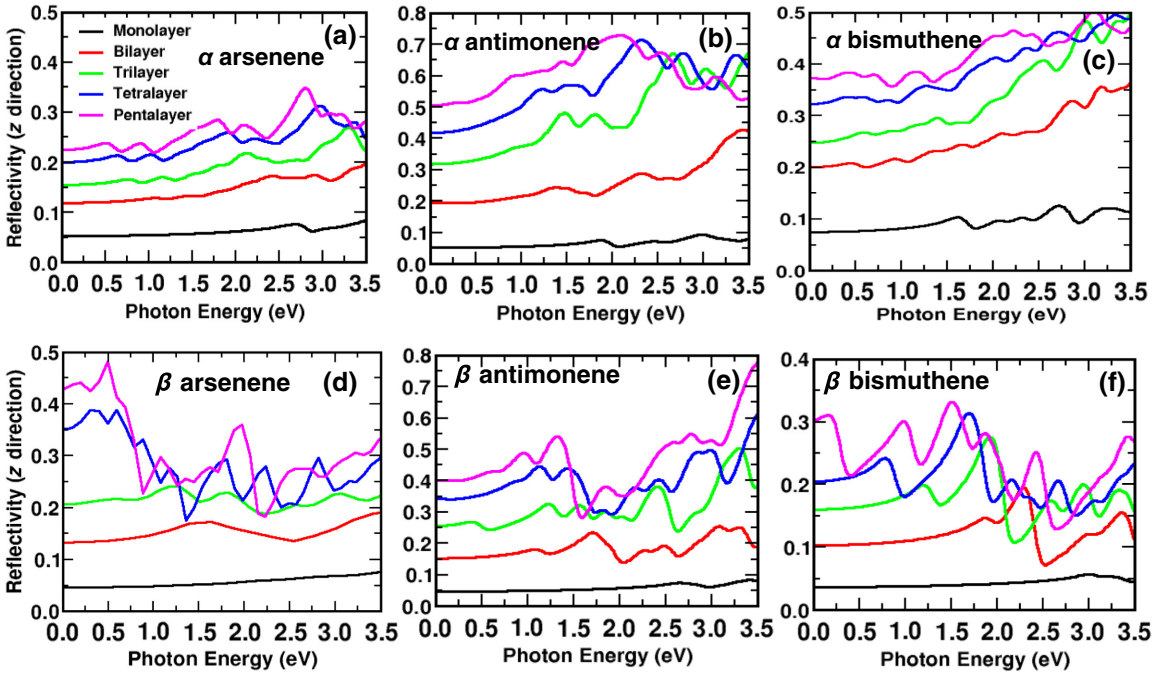

FIG. 8. Reflectivity spectra of the out-of-plane polarization for various layered structures of (a)–(c) α and (d)–(f) β allotropes of arsenene, antimonene, and bismuthene, calculated with use of the HSE06 hybrid functional.

and β allotropes of arsenene, antimonene, and bismuthene. For monolayers, the reflectivity in the visible region is approximately 5%. As we see from Fig. 7, the absorption is negligible in the visible region, which confirms that the group-V monoelemental monolayers are suitable candidates for transparent materials. The reflectivity increases in the higher-photon-energy range. Also, as we move from a monolayer to a pentalayer, the reflectivity increases gradually due to the reduction in the band gap. However, the absorption remains negligible in the visible region. This is attributed to the strong excitonic effects generally observed in low-dimensional (2D) materials arising from quantum confinement. The exciton binding energies are large in atomically thin semiconducting (2D) materials, and this has a pronounced effect on the dielectric function [70–72]. Recently, it was shown that exciton binding energy is almost inversely proportional to static polarizability for 2D materials [73,74]. To analyze the dependence of the excitonic effect on the layer thickness of group-V 2D systems, we calculate their exciton binding energies up to the trilayered structure using the BSE method. Although BSE calculations are highly accurate, they are computationally quite expensive; hence, we perform calculations up to only the trilayered structure. This, however, gives a reasonable indication of the variation of excitonic effects with change in layer thickness. Table IV gives the calculated exciton binding energies for a monolayer, bilayer, and trilayer of the two allotropes of the three materials. The exciton binding energies range from 0.27 to 1.61 eV, which indicates a reasonably strong excitonic effect in these thin 2D films. As expected, with increasing number of layers, the exciton binding energy decreases, which consequently causes an increase in the polarizability. This might explain the increase in reflectivity with increasing layer thickness [70]. In the case of α-arsenene, the reflectivity is below 20% up to the trilayered structure in the visible region [see Fig. 8(a)]. Hence, trilayered α-arsenene is the best candidate as a transparent layer for solar PV devices. Similarly, multilayered slabs up to the tetralayered structure for β-arsenene and up to the bilayered structure for antimonene (for the α and β allotropes) can be considered to be used as a transparent layer [reflectivity less than 20%; see Fig. 8(d)]. However, for bismuthene, any surface slab beyond the bilayered structure may not be a good candidate for a transparent conducting layer.

TABLE IV. Exciton binding energy (in eV) for a monolayer, bilayer, and trilayer of the α and β allotropes of arsenene, antimonene, and bismuthene. The calculations are done with the BSE method.

Allotrope	Monolayer	Bilayer	Trilayer
α-Arsenene	0.72	0.63	0.49
α-Antimonene	0.42	0.34	0.27
α-Bismuthene	0.78	0.51	0.34
β-Arsenene	1.61	0.83	0.58
β-Antimonene	0.74	0.52	0.33
β-Bismuthene	0.84	0.67	0.53

D. Carrier transport in α-arsenene, β-arsenene, α-antimonene, β-antimonene, α-bismuthene, and β-bismuthene

Understanding carrier-transport mechanisms is essential for a transparent-conducting-material electrode. In this subsection, we present the results of a study of temperature-dependent carrier transport in the group-V 2D monolayers. Figures 9(a)–9(f) and 10(a)–10(c) show the temperature dependence of the in-plane electrical conductivity (σ) for the α and β allotropes of arsenene, antimonene, and bismuthene monolayers. The α allotrope is structurally anisotropic, unlike its β counterpart, and hence the former has unequal xx and yy components of conductivity. σ is calculated for different dopant concentrations in the range from 10^{20} to 10^{21} cm^{-3}. The carrier relaxation time (τ) for α and β allotropes of the three materials is shown in Figs. 9(g)–9(i) and 10(d)–10(f), respectively. As is evident, the relaxation time for all three materials ranges between 1 and 70 fs. For the α allotropes, the conductivity for the x and y directions increases in the low-temperature range (25–50 K) for all dopant concentrations. This is because the carrier concentration increases in this temperature range, and dominates over the appreciable effect due to ionized-impurity scattering. Beyond 50 K, the carrier concentration starts to be saturated, while the relaxation time decreases. This causes an overall reduction in conductivity, suggesting a semiconductor-to-metallic transition at 50 K. The reduction in relaxation time mainly arises due to the dominant effect of ADP scattering. For α-bismuthene [see Figs. 9(c) and 9(f)], certain bumps are observed in the conductivity in the temperature range from 400 to 500 K for dopant concentrations of 10×10^{20}, 15×10^{20}, and 20×10^{20} cm^{-3}. An enlarged view of σ-versus-T plots in the temperature range from 400 to 600 K with a smaller step of 10 K is shown in Fig. S4 in Supplemental Material [55]. A closer look at these plots shows that σ increases between 450 and 460 K and then decreases for dopant concentrations of 10×10^{20}, 15×10^{20}, and 20×10^{20} cm^{-3} in the x and y directions. Such anomalous behavior might arise due

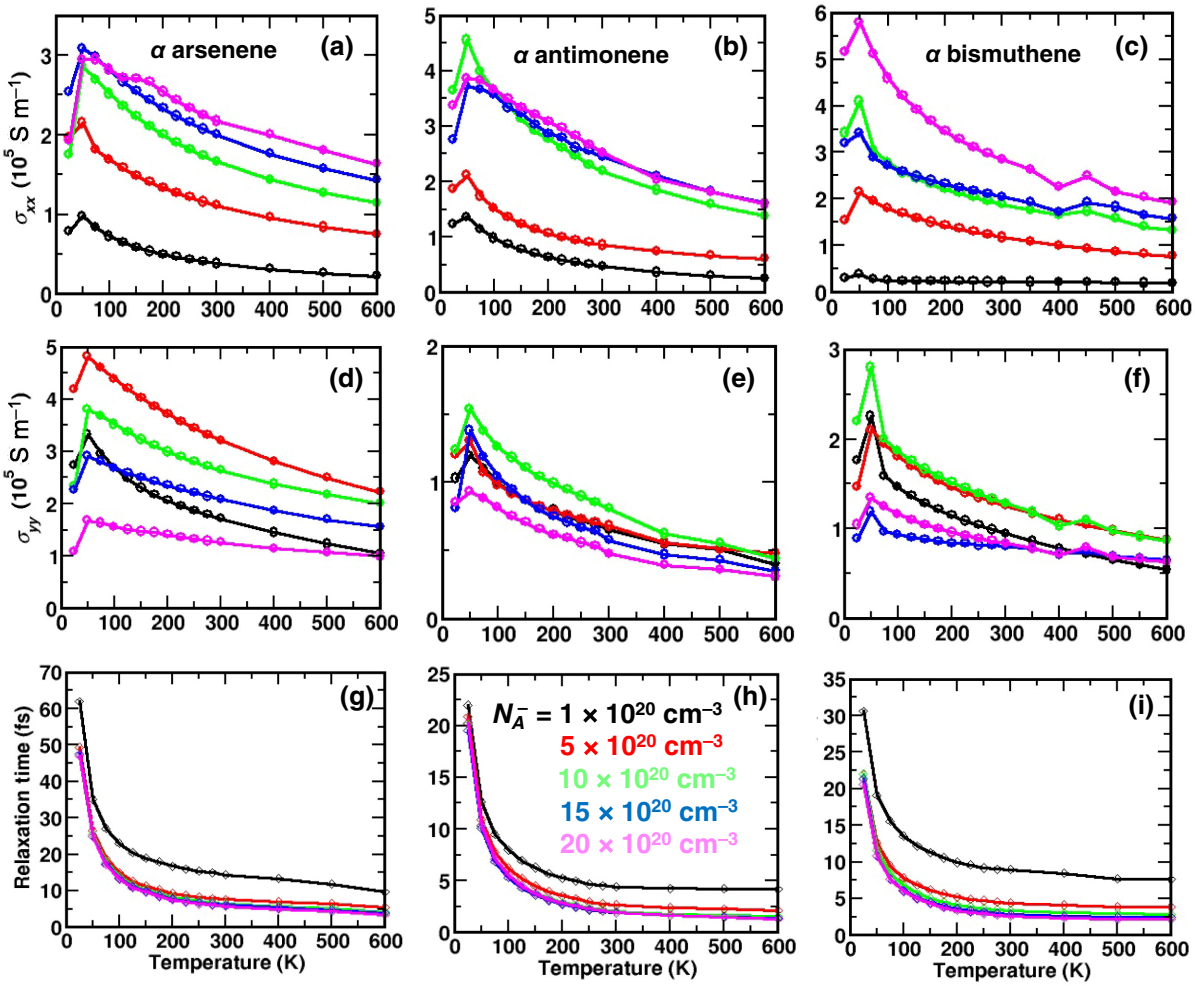

FIG. 9. Temperature and carrier-concentration (N_A^-) dependence of the electrical conductivity (σ) in the xx and yy directions, and the carrier relaxation time (τ) for (a),(d),(g) α-arsenene, (b),(e),(h) α-antimonene, and (c),(f),(i) α-bismuthene monolayers.

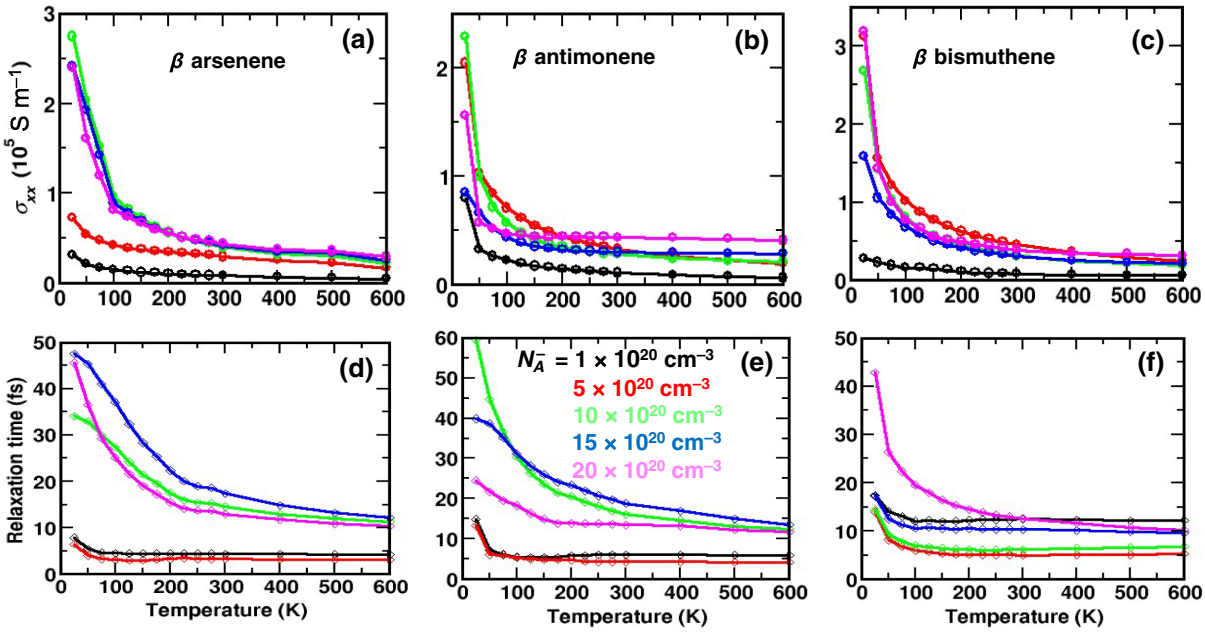

FIG. 10. (Temperature and carrier-concentration (N_A^-) dependence of the electrical conductivity (σ) and the carrier relaxation time (τ) for (a),(d) β-arsenene (b),(e) β-antimonene, and (c),(f) β-bismuthene monolayers. The conductivity in the xx and yy directions is the same in this case due to structural symmetry.

to the anisotropic nature of the relaxation time. Note that the relaxation time shown in Fig. 9 includes the effect of impurity-ionization scattering only. In a real 2D material, however, other scattering mechanisms that vary drastically at different dopant concentrations are also involved. This might play an important role because the relaxation time showing anisotropic behavior causes anomalous conductivity in 2D systems [75–77]. We speculate that this kind of σ-versus-T behavior may be associated with some kind of phase transition (arising from structural or chemical environment changes) between 450 and 460 K for α-bismuthene.

Unlike the α allotropes, the conductivity of the β allotropes decreases with increasing temperature in the entire temperature range. In this case, ADP scattering is the dominant scattering, which is confirmed by the relaxation-time plots [see Figs. 10(d)–10(f)]. The conductivity of all the group-V-element monolayers is found to be reasonably high (approximately 10^5 S m^{-1}). The α allotropes are relatively more conducting than the β ones. To gain further insight, we also calculate the conductivity of the α and β allotropes of bilayered arsenene and the α allotrope of trilayered arsenene (see Sec. 5 in Supplemental Material [55] for more details). Similarly to for monolayered α-arsenene, a semiconductor-to-metallic transition occurs at 50 K, beyond which the conductivity decreases monotonously (see Figs. S5.1 and S5.2 in Supplemental Material [55]). Interestingly, the conductivity increases with increasing layer thickness. To check their performance as a transparent conducting layer, we calculate the figure of merit

TABLE V. Figure of merit (FOM) for the α and β allotropes of arsenene, antimonene, and bismuthene. R, α, $\mathcal{T}$, σ, and R_{sh} are the reflectivity, absorption coefficient, transmittance, electrical conductivity, and sheet resistance, respectively. 1L, monolayer; 2L, bilayer; 3L, trilayer.

Allotrope	Thickness (t) (Å)	R	α (10^4 cm^{-1})	$\mathcal{T}$	σ (S m^{-1}) at 300 K	$R_{sh} = (\sigma t)^{-1}$ (Ω/□)	FOM $= \mathcal{T}^{10}/R_{sh}$ (mS)
α-Arsenene (1L)	2.38	0.05	0.01	0.95	1.66×10^5	2.53×10^4	0.02
α-Arsenene (2L)	7.91	0.13	0.01	0.87	2.97×10^5	0.42×10^4	0.06
α-Arsenene (3L)	13.47	0.15	0.01	0.85	5.41×10^5	0.13×10^4	0.15
α-Antimonene (1L)	2.79	0.05	0.01	0.95	2.18×10^5	1.64×10^4	0.03
α-Bismuthene (1L)	2.95	0.07	0.01	0.93	1.88×10^5	1.80×10^4	0.02
β-Arsenene (1L)	1.40	0.04	0.01	0.96	0.41×10^5	4.24×10^4	0.01
β-Arsenene (2L)	5.74	0.12	0.01	0.88	0.87×10^5	2.00×10^4	0.01
β-Antimonene (1L)	1.64	0.05	0.01	0.95	0.27×10^5	2.25×10^4	0.02
β-Bismuthene (1L)	1.71	0.07	0.01	0.93	0.31×10^5	1.83×10^4	0.02

(FOM) for all our 2D systems using the relation proposed by Haacke [78], FOM $= T^{10}/R_{sh}$, where R_{sh} is the sheet resistance. The calculated FOM values are listed in Table V. The FOM for the best-performing material, trilayered α-arsenene, is 0.15 mS. Our calculated FOM values of these group-V 2D layered structures are about 1 or 2 orders less than those of the state-of-the-art transparent conducting layers used in solar PV devices such as indium tin oxide (ITO) and fluorine-doped tin oxide (FTO) [79–82]. The low FOM is mainly attributed to the smaller thickness of these 2D films causing the high sheet resistance. Therefore, among the group-V 2D structures, we propose trilayered α-arsenene as a promising candidate for a transparent conducting layer.

IV. CONCLUSIONS

In summary, we systematically investigate the thickness (multilayer) dependence of the electronic structure and the optical and carrier-transport properties of highly stable α and β allotropes of arsenene, antimonene, and bismuthene from a monolayer to a pentalayer using first-principles calculations. This study helps us to identify an optimal thickness of these 2D systems for further experimental analysis. The electronic band structures suggest that the monolayers of α and β allotropes are semiconducting, with a band gap ranging between 0.27 and 2.28 eV. The band gap of α-bismuthene and β-bismuthene is direct, while that of arsenene and antimonene is indirect. Simulation of multilayered structures confirms a reduction in band gap with increasing layer thickness due to the interlayer interaction between the p_z orbitals of adjacent layers. α-Arsenene shows semiconducting behavior throughout, from a monolayer to a pentalayer. However, for β-arsenene, only the monolayered and the bilayered structures are semiconducting, while the rest of the higher-order layers of β-arsenene as well as antimonene and bismuthene show metallic character. The peaks in the imaginary part of the dielectric function of all the materials correspond well to the interband transitions of electrons from the valence band to the conduction band. The simulated absorption coefficient and reflectivity spectra for both allotropes of the three monolayered materials confirm them to be potential candidates for transparent conducting layers (reflectivity of 5% or less). The simulated electrical conductivity for all the materials lies in the range from 10^4 to 10^5 S m^{-1}. The FOM of the best-performing material, trilayered α-arsenene, is 0.15 mS. A combined evaluation of carrier-transport and optical properties suggests that trilayered α-arsenene may be a suitable candidate for transparent conducting layers in photovoltaic applications, requiring further experimental investigation.

ACKNOWLEDGMENTS

G.B. thanks the Council of Scientific and Industrial Research, India, for providing a senior research fellowship. The authors thank Dr. Garima Aggarwal for fruitful discussion. A.A. thanks S. Mahapatra for initial discussion on this topic. This work was performed as part of the National Centre for Photovoltaic Research and Education Phase 2, funded by the Ministry of New and Renewable Energy, Government of India, at IIT Bombay.

[1] Y. Liu, N. O. Weiss, X. Duan, H.-C. Cheng, Y. Huang, and X. Duan, Van der Waals heterostructures and devices, Nat. Rev. Mater. **1**, 1 (2016).

[2] M. Pumeraand and Z. Sofer, 2D monoelemental arsenene, antimonene, and bismuthene: Beyond black phosphorus, Adv. Mater. **29**, 1605299 (2017).

[3] D. Xiao, G.-B. Liu, W. Feng, X. Xu, and W. Yao, Coupled Spin and Valley Physics in monolayers of MoS_2 and Other Group-VI Dichalcogenides, Phys. Rev. Lett. **108**, 196802 (2012).

[4] K. S. Novoselov, A. K. Geim, S. V. Morozov, D. Jiang, Y. Zhang, S. V. Dubonos, I. V. Grigorieva, and A. A. Firsov, Electric field effect in atomically thin carbon films, Science **306**, 666 (2004).

[5] S. Zhang, S. Guo, Z. Chen, Y. Wang, H. Gao, J. Gómez-Herrero, P. Ares, F. Zamora, Z. Zhu, and H. Zeng, Recent progress in 2D group-VA semiconductors: from theory to experiment, Chem. Soc. Rev. **47**, 982 (2018).

[6] E. Durgun, S. Tongay, and S. Ciraci, Silicon and III-V compound nanotubes: Structural and electronic properties, Phys. Rev. B **72**, 075420 (2005).

[7] K. K. Kim, A. Hsu, X. Jia, S. M. Kim, Y. Shi, M. Hofmann, D. Nezich, J. F. Rodriguez-Nieva, M. Dresselhaus, and T. Palacios, *et al.*, Synthesis of monolayer hexagonal boron nitride on Cu foil using chemical vapor deposition, Nano Lett. **12**, 161 (2012).

[8] S. Cahangirov, M. Topsakal, and S. Ciraci, Armchair nanoribbons of silicon and germanium honeycomb structures, Phys. Rev. B **81**, 195120 (2010).

[9] H. Şahin, S. Cahangirov, M. Topsakal, E. Bekaroglu, E. Akturk, R. T. Senger, and S. Ciraci, Monolayer honeycomb structures of group-IV elements and III-V binary compounds: First-principles calculations, Phys. Rev. B **80**, 155453 (2009).

[10] D. Kecik, A. Onen, M. Konuk, E. Gürbüz, F. Ersan, S. Cahangirov, E. Aktürk, E. Durgun, and S. Ciraci, Fundamentals, progress, and future directions of nitride-based semiconductors and their composites in two-dimensional limit: A first-principles perspective to recent synthesis, Appl. Phys. Rev. **5**, 011105 (2018).

[11] D. Kecik, V. Özçelik, E. Durgun, and S. Ciraci, Structure dependent optoelectronic properties of monolayer antimonene, bismuthene and their binary compound, Phys. Chem. Chem. Phys. **21**, 7907 (2019).

[12] A. C. Neto, F. Guinea, N. M. Peres, K. S. Novoselov, and A. K. Geim, The electronic properties of graphene, Rev. Mod. Phys. **81**, 109 (2009).

[13] Q. Peng, A. K. Dearden, J. Crean, L. Han, S. Liu, X. Wen, and S. De, New materials graphyne, graphdiyne, graphone, and graphane: Review of properties, synthesis, and

application in nanotechnology, Nanotechnol. Sci. Appl. **7**, 1 (2014).
[14] P. Jamdagni, A. Thakur, A. Kumar, P. Ahluwalia, and R. Pandey, Two dimensional allotropes of arsenene with a wide range of high and anisotropic carrier mobility, Phys. Chem. Chem. Phys. **20**, 29939 (2018).
[15] B. Zhang, H. Zhang, J. Lin, and X. Cheng, First-principle study of seven allotropes of arsenene and antimonene: Thermodynamic, electronic and optical properties, Phys. Chem. Chem. Phys. **20**, 30257 (2018).
[16] S. Zhang, Z. Yan, Y. Li, Z. Chen, and H. Zeng, Atomically thin arsenene and antimonene: semimetal–semiconductor and indirect–direct band-gap transitions, Angew. Chem. **127**, 3155 (2015).
[17] J. Shah, W. Wang, H. M. Sohail, and R. Uhrberg, Experimental evidence of monolayer arsenene: An exotic 2D semiconducting material, 2D Mater. **7**, 025013 (2020).
[18] Z. Wuand and J. Hao, Electrical transport properties in group-V elemental ultrathin 2D layers, npj 2D Mater. Appl. **4**, 1 (2020).
[19] S. Mardanya, V. K. Thakur, S. Bhowmick, and A. Agarwal, Four allotropes of semiconducting layered arsenic that switch into a topological insulator via an electric field: Computational study, Phys. Rev. B **94**, 035423 (2016).
[20] R. Feiand and L. Yang, Strain-engineering the anisotropic electrical conductance of few-layer black phosphorus, Nano Lett. **14**, 2884 (2014).
[21] J. Qiao, X. Kong, Z.-X. Hu, F. Yang, and W. Ji, High-mobility transport anisotropy and linear dichroism in few-layer black phosphorus, Nat. Commun. **5**, 1 (2014).
[22] L. Li, Y. Yu, G. J. Ye, Q. Ge, X. Ou, H. Wu, D. Feng, X. H. Chen, and Y. Zhang, Black phosphorus field-effect transistors, Nat. Nanotechnol. **9**, 372 (2014).
[23] Q. Liu, X. Zhang, L. Abdalla, A. Fazzio, and A. Zunger, Switching a normal insulator into a topological insulator via electric field with application to phosphorene, Nano Lett. **15**, 1222 (2015).
[24] Z. Zhang, J. Xie, D. Yang, Y. Wang, M. Si, and D. Xue, Manifestation of unexpected semiconducting properties in few-layer orthorhombic arsenene, Appl. Phys. Exp. **8**, 055201 (2015).
[25] M. Zhao, X. Zhang, and L. Li, Strain-driven band inversion and topological aspects in antimonene, Sci. Rep. **5**, 1 (2015).
[26] B. Peng, H. Zhang, H. Shao, K. Xu, G. Ni, J. Li, H. Zhu, and C. M. Soukoulis, Chemical intuition for high thermoelectric performance in monolayer black phosphorus, α-arsenene and aW-antimonene, J. Mater. Chem. A **6**, 2018 (2018).
[27] E. Aktürk, O. Ü. Aktürk, and S. Ciraci, Single and bilayer bismuthene: Stability at high temperature and mechanical and electronic properties, Phys. Rev. B **94**, 014115 (2016).
[28] Y. Xu, B. Peng, H. Zhang, H. Shao, R. Zhang, and H. Zhu, First-principle calculations of optical properties of monolayer arsenene and antimonene allotropes, Ann. Phys. **529**, 1600152 (2017).
[29] D. Singh, S. K. Gupta, Y. Sonvane, and I. Lukačević, Antimonene: A monolayer material for ultraviolet optical nanodevices, J. Mater. Chem. C **4**, 6386 (2016).
[30] P. Yuan, T. Zhang, J. Sun, L. Liu, Y. Yao, and Y. Wang, Recent progress in 2D group-V elemental monolayers: Fabrications and properties, J. Semicond. **41**, 081003 (2020).
[31] H. Shu, Y. Li, X. Niu, and J. Guo, Electronic structures and optical properties of arsenene and antimonene under strain and an electric field, J. Mater. Chem. C **6**, 83 (2018).
[32] X. Wu, Y. Shao, H. Liu, Z. Feng, Y.-L. Wang, J.-T. Sun, C. Liu, J.-O. Wang, Z.-L. Liu, and S.-Y. Zhu, *et al.*, Epitaxial growth and air-stability of monolayer antimonene on $PdTe_2$, Adv. Mater. **29**, 1605407 (2017).
[33] T. Nagao, T. Doi, T. Sekiguchi, and S. Hasegawa, Epitaxial growth of single-crystal ultrathin films of bismuth on Si(111), Jpn. J. Appl. Phys. **39**, 4567 (2000).
[34] P. Ares, F. Aguilar-Galindo, D. Rodríguez-San-Miguel, D. A. Aldave, S. Díaz-Tendero, M. Alcami, F. Martín, J. Gómez-Herrero, and F. Zamora, Mechanical isolation of highly stable antimonene under ambient conditions, Adv. Mater. **28**, 6332 (2016).
[35] H.-S. Tsai, C.-W. Chen, C.-H. Hsiao, H. Ouyang, and J.-H. Liang, The advent of multilayer antimonene nanoribbons with room temperature orange light emission, Chem. Commun. **52**, 8409 (2016).
[36] P. Hohenbergand and W. Kohn, Density functional theory (DFT), Phys. Rev. **136**, B864 (1964).
[37] G. Kresseand and J. Furthmüller, Efficiency of ab-initio total energy calculations for metals and semiconductors using a plane-wave basis set, Comput. Mater. Sci. **6**, 15 (1996).
[38] G. Kresseand and J. Hafner, Ab initio molecular dynamics for liquid metals, Phys. Rev. B **47**, 558 (1993).
[39] G. Kresseand and J. Furthmüller, Efficient iterative schemes for ab initio total-energy calculations using a plane-wave basis set, Phys. Rev. B **54**, 11169 (1996).
[40] P. E. Blöchl, Projector augmented-wave method, Phys. Rev. B **50**, 17953 (1994).
[41] J. P. Perdew, K. Burke, and M. Ernzerhof, Generalized Gradient Approximation Made Simple [Phys. Rev. Lett. 77, 3865 (1996)], Phys. Rev. Lett. **78**, 1396 (1997).
[42] J. P. Perdew, K. Burke, and M. Ernzerhof, Generalized Gradient Approximation Made Simple, Phys. Rev. Lett. **77**, 3865 (1996).
[43] J. Heyd, G. E. Scuseria, and M. Ernzerhof, Hybrid functionals based on a screened Coulomb potential, J. Chem. Phys. **118**, 8207 (2003).
[44] J. Heydand and G. E. Scuseria, Efficient hybrid density functional calculations in solids: Assessment of the Heyd–Scuseria–Ernzerhof screened Coulomb hybrid functional, J. Chem. Phys. **121**, 1187 (2004).
[45] S. Grimme, Semiempirical GGA-type density functional constructed with a long-range dispersion correction, J. Comput. Chem. **27**, 1787 (2006).
[46] P. E. Blöchl, O. Jepsen, and O. K. Andersen, Improved tetrahedron method for Brillouin-zone integrations, Phys. Rev. B **49**, 16223 (1994).
[47] M. Gajdoš, K. Hummer, G. Kresse, J. Furthmüller, and F. Bechstedt, Linear optical properties in the projector-augmented wave methodology, Phys. Rev. B **73**, 045112 (2006).
[48] S. L. Adler, Quantum theory of the dielectric constant in real solids, Phys. Rev. **126**, 413 (1962).
[49] N. Wiser, Dielectric constant with local field effects included, Phys. Rev. **129**, 62 (1963).
[50] S. Albrecht, L. Reining, R. Del Sole, and G. Onida, Ab Initio Calculation of Excitonic Effects in the Optical

Spectra of Semiconductors, Phys. Rev. Lett. **80**, 4510 (1998).
[51] M. Rohlfingand and S. G. Louie, Electron-Hole Excitations in Semiconductors and Insulators, Phys. Rev. Lett. **81**, 2312 (1998).
[52] Y.-M. Byunand and C. A. Ullrich, Assessment of long-range-corrected exchange-correlation kernels for solids: Accurate exciton binding energies via an empirically scaled bootstrap kernel, Phys. Rev. B **95**, 205136 (2017).
[53] T. Sander, E. Maggio, and G. Kresse, Beyond the Tamm-Dancoff approximation for extended systems using exact diagonalization, Phys. Rev. B **92**, 045209 (2015).
[54] A. M. Ganose, J. Park, A. Faghaninia, R. Woods-Robinson, K. A. Persson, and A. Jain, Efficient calculation of carrier scattering rates from first principles, Nat. Commun. **12**, 1 (2021).
[55] See Supplemental Material at http://link.aps.org/supplemental/10.1103/PhysRevApplied.19.054068 for the thickness-dependent electronic band structures and density of states for the α and β allotropes of antimonene and bismuthene, the in-plane conductivity of α-bismuthene in the temperature range from 400 to 600 K, and bilayered and trilayered α-arsenene and β-arsenene.
[56] M. Dresselhaus, *et al.*, Solid state physics part II optical properties of solids, Lect. Notes (Massachusetts Institute of Technology, Cambridge, MA) **17**, 15 (2001).
[57] G. Brunin, F. Ricci, V.-A. Ha, G.-M. Rignanese, and G. Hautier, Transparent conducting materials discovery using high-throughput computing, npj Comput. Mater. **5**, 63 (2019).
[58] H. Peelaers, E. Kioupakis, and C. Van de Walle, Free-carrier absorption in transparent conducting oxides: Phonon and impurity scattering in SnO_2, Phys. Rev. B **92**, 235201 (2015).
[59] P. P. Edwards, A. Porch, M. O. Jones, D. V. Morgan, and R. M. Perks, Basic materials physics of transparent conducting oxides, Dalton Trans. **19**, 2995 (2004).
[60] M. Chen, Z. Pei, X. Wang, Y. Yu, X. Liu, C. Sun, and L. Wen, Intrinsic limit of electrical properties of transparent conductive oxide films, J. Phys. D: Appl. Phys. **33**, 2538 (2000).
[61] G. K. Madsenand and D. J. Singh, BoltzTraP. A code for calculating band-structure dependent quantities, Compt. Phys. Commun. **175**, 67 (2006).
[62] L. Hu, Z. Xu, F. Long, J. Yuan, H. Li, A. Zhao, S.-T. Han, N. Zhang, X. Liu, and C. Ma, *et al.*, Direct bandgap opening in sodium-doped antimonene quantum dots: An emerging 2D semiconductor, Mater. Horiz. **7**, 1588 (2020).
[63] I. Aguilera, C. Friedrich, and S. Blügel, Electronic phase transitions of bismuth under strain from relativistic self-consistent GW calculations, Phys. Rev. B **91**, 125129 (2015).
[64] L. Paulingand and M. L. Huggins, Covalent radii of atoms and interatomic distances in crystals containing electron-pair bonds, Z. für Kristallogr.-Cryst. Mater. **87**, 205 (1934).
[65] Y. Kadioglu, J. A. Santana, H. D. Özaydin, x. Ersan, O. Ü. Aktürk, E. Aktürk, and F. A. Reboredo, Diffusion quantum Monte Carlo and density functional calculations of the structural stability of bilayer arsenene, J. Chem. Phys. **148**, 214706 (2018).
[66] K. Mi, J. Xie, M. Si, and C. Gao, Layer-stacking effect on electronic structures of bilayer arsenene, Europhys. Lett. **117**, 27002 (2017).
[67] A. L. Elías, N. Perea-López, A. Castro-Beltrán, A. Berkdemir, R. Lv, S. Feng, A. D. Long, T. Hayashi, Y. A. Kim, and M. Endo, *et al.*, Controlled synthesis and transfer of large-area WS_2 sheets: From single layer to few layers, ACS Nano **7**, 5235 (2013).
[68] S. Choi, Z. Shaolin, and W. Yang, Layer-number-dependent work function of MoS_2 nanoflakes, J. Korean Phys. Soc. **64**, 1550 (2014).
[69] W. Zhao, R. M. Ribeiro, M. Toh, A. Carvalho, C. Kloc, A. Castro Neto, and G. Eda, Origin of indirect optical transitions in few-layer MoS_2, WS_2, and WSe_2, Nano Lett. **13**, 5627 (2013).
[70] Y. Yu, Y. Yu, Y. Cai, W. Li, A. Gurarslan, H. Peelaers, D. E. Aspnes, C. G. Van de Walle, N. V. Nguyen, and Y.-W. Zhang, *et al.*, Exciton-dominated dielectric function of atomically thin MoS_2 films, Sci. Rep. **5**, 1 (2015).
[71] K. F. Mak, C. Lee, J. Hone, J. Shan, and T. F. Heinz, Atomically Thin MoS_2: A new direct-gap semiconductor, Phys. Rev. Lett. **105**, 136805 (2010).
[72] Q. H. Wang, K. Kalantar-Zadeh, A. Kis, J. N. Coleman, and M. S. Strano, Electronics and optoelectronics of two-dimensional transition metal dichalcogenides, Nat. Nanotechnol. **7**, 699 (2012).
[73] T. Olsen, S. Latini, F. Rasmussen, and K. S. Thygesen, Simple Screened Hydrogen Model of Excitons in Two-Dimensional Materials, Phys. Rev. Lett. **116**, 056401 (2016).
[74] G. Zhang, A. Chaves, S. Huang, F. Wang, Q. Xing, T. Low, and H. Yan, Determination of layer-dependent exciton binding energies in few-layer black phosphorus, Sci. Adv. **4**, eaap9977 (2018).
[75] S. Zhao, B. Dong, H. Wang, H. Wang, Y. Zhang, Z. V. Han, and H. Zhang, In-plane anisotropic electronics based on low-symmetry 2D materials: progress and prospects, Nanoscale Adv. **2**, 109 (2020).
[76] H. Lang, S. Zhang, and Z. Liu, Mobility anisotropy of two-dimensional semiconductors, Phys. Rev. B **94**, 235306 (2016).
[77] W.-G. Lee, Y. K. Chung, J. Lee, B. J. Kim, S. Chae, B. J. Jeong, J.-Y. Choi, and J. Huh, Edge defect-free anisotropic two-dimensional sheets with nearly direct band gaps from a true one-dimensional van der Waals Nb_2Se_9 material, ACS Omega **5**, 10800 (2020).
[78] G. Haacke, New figure of merit for transparent conductors, J. Appl. Phys. **47**, 4086 (1976).
[79] T. Kawashima, T. Ezure, K. Okada, H. Matsui, K. Goto, and N. Tanabe, FTO/ITO double-layered transparent conductive oxide for dye-sensitized solar cells, J. Photochem. Photobiol. A **164**, 199 (2004).
[80] W.-J. Choi, D.-J. Kwak, C.-S. Park, and Y.-M. Sung, Characterization of transparent conductive ITO, ITiO, and FTO films for application in photoelectrochemical cells, J. Nanosci. Nanotechnol. **12**, 3394 (2012).
[81] D. S. Ginleyand and C. Bright, Transparent conducting oxides, MRS Bull. **25**, 15 (2000).
[82] C. Sima, C. Grigoriu, and S. Antohe, Comparison of the dye-sensitized solar cells performances based on transparent conductive ITO and FTO, Thin Solid Films **519**, 595 (2010).